*photonics*

MDPI

*Article*

# All-Chalcogenide High-NA Broadband Achromatic Metalens for Long-Wavelength Infrared Regime

**Minsi Lin [1,†], Zhenqi Huang [1,†], Yue Shen [1], Haobin Xiao [1], Yingying Fu [1], Mingjie Zhang [1,*], Yuanzhi Chen [2,*], Yi Zhou [3], Siqi Zhu [1] and Zhenqiang Chen [1]**

[1] College of Physics and Optoelectronic Engineering, Jinan University, Guangzhou 510632, China; linminsi@stu.jnu.edu.cn (M.L.); hzq0459@stu2022.jnu.edu.cn (Z.H.); 1.shenyue@stu2023.jnu.edu.cn (Y.S.); xxx07@stu2024.jnu.edu.cn (H.X.); fuyingying@stu2025.jnu.edu.cn (Y.F.); tzhusiqi@jnu.edu.cn (S.Z.); zqchen@jnu.edu.cn (Z.C.)
[2] School of Material Science and Engineering, Shanghai Institute of Technology, Shanghai 201418, China
[3] Guangzhou Idealmeta Technology Co., Ltd., Guangzhou 510000, China; tiger.zhou@idealmeta.com.cn
* Correspondence: mjzhang@jnu.edu.cn (M.Z.); yzchen@sit.edu.cn (Y.C.)
† These authors contributed equally to this work.

**Abstract**

The long-wave infrared band, which at room temperature covers the infrared radiation of humans and objects, has significant applications across various fields including wireless communication, national defense, military, biomedical, and advanced driver assistance systems. Metalens provides a pathway to lightweight, compact, and integrated solutions for infrared imaging and sensing systems, marking an inevitable trend in future development. This study presents a design for a high numerical aperture of 0.89 in a polarization-insensitive all-chalcogenide metalens operating at 10 μm, utilizing the commercially available chalcogenide glass material $As_2Se_3$ via a transmission phase approach. Building upon this, we have achieved, for the first time, a high numerical aperture of 0.84 for an all-chalcogenide broadband LWIR achromatic metalens operating in the 9.5–10.5 μm range, with significantly improved focusing performance through the application of particle swarm optimization algorithms. The superior performance of the all-chalcogenide LWIR metalens, combined with the advantages of chalcogenide glass over traditional LWIR materials such as Si or Ge—namely, lower cost, reduced optical loss, and a smaller thermo-optic coefficient—suggests it has significant potential for broader applications.

**Keywords:** metalens; chalcogenide glass; long-wavelength infrared; achromatic

## 1. Introduction

The long-wavelength infrared (LWIR) band, spanning 8 μm to 12 μm and situated within the atmospheric low-loss transmission window, is crucial for various applications such as wireless communication, defense and military operations, biomedicine, environmental sensing, and assisted driving due to its coverage of infrared radiation from both humans and objects at room temperature [1,2]. For instance, in recent years, LWIR thermal imaging and temperature measurement systems have made outstanding contributions to curbing the rampant spread of the novel coronavirus infection (COVID-19) worldwide. LWIR optical lenses play an indispensable role in the discrete manipulation of LWIR wavefronts, making them crucial for LWIR thermal imaging and temperature measurement [3,4]. However, traditional refractive optical lenses typically exhibit characteristics such as surface curvature and macroscopic scale, which impose significant spatial requirements and

Check for updates

Received: 30 March 2026
Revised: 21 April 2026
Accepted: 23 April 2026
Published: 28 April 2026

**Copyright:** © 2026 by the authors. Licensee MDPI, Basel, Switzerland. This article is an open access article distributed under the terms and conditions of the Creative Commons Attribution (CC BY) license.

high environmental stability demands, constrained by optical diffraction limits, imaging conditions, and material optical parameters [5]. Achieving satisfactory optical imaging under the limitations of optical material dispersion and off-axis conditions often necessitates elaborate designs of multiple lens combinations to correct for chromatic aberration and aberrations, inevitably leading to increased system volume, weight, and cost [6,7]. This undoubtedly fails to align with the current trends of lightweight, miniaturized, and integrated devices and equipment, which will inevitably limit their application scope.

Metasurfaces, emerging as a novel method for electromagnetic wave manipulation, are two-dimensional metamaterials formed by arranging subwavelength-scale planar artificial atoms in specific sequences [8,9]. Through careful design and tailoring of the geometric dimensions, spatial orientations, arrangements, and periodicities of artificial atoms (micro/nanostructures), metasurfaces enable multidimensional arbitrarily control over light, including phase, polarization, and amplitude. This capability significantly caters to the growing demand for miniaturized, lightweight, highly integrated, and multifunctional photonic devices in the backdrop of rapid advancements in information technologies such as artificial intelligence (AI), 5G communication, and high-end chip manufacturing. Since their inception, meta-surfaces have become a focal point of research in various related disciplines. To date, leveraging meta-surfaces for flexible modulation of electromagnetic wave fronts has facilitated applications such as optical holography [10–12], vortex beam generators [13–15], perfect absorbers [16–18], and metalens [19–21]. Among these applications, metalens utilizing the phase gradient introduced by microstructures, as described in the generalized Snell's law 9, exhibit controlled deflection of incident light. This fundamentally addresses the challenges associated with traditional lens systems, such as low spatial light modulation efficiency and constraints on miniaturization and microscale integration. Consequently, metalens presents a promising flat and lightweight alternative for optical system design. Additionally, their compatibility with semiconductor fabrication processes enables on-chip integration and large-scale manufacturing, significantly reducing the manufacturing costs of optical systems. To further enhance the performance of metalens-based systems, achromatic metalenses, leveraging the immense flexibility and optical manipulation capabilities of metasurfaces, have evolved from achieving achromaticity at a few discrete wavelengths [22,23] or narrow bandwidths [24,25] to achieving broadband achromaticity [26,27]. However, despite the exciting progress in metalens research, existing studies on metalens and achromatic metalens have primarily focused on the visible [5,26–28] or near-infrared (NIR) [29,30] regions, with relatively less attention given to the mid-wave infrared (MWIR) [31–33] and LWIR [34–36] band, especially the LWIR. This limitation is likely due to the limited selection of materials suitable for the LWIR, as well as the manufacturing challenges associated with the compared high aspect ratio micro/nanostructures required for LWIR metalens. Most classical optical materials, such as oxide glasses and polymers, are unsuitable for operation in the LWIR region due to phonon absorption. Only a limited number of materials, including single-crystal Ge, Si, ZnSe, $CaF_2$, $BaF_2$, and chalcogenide glasses, are transparent in LWIR. Among these few materials, ZnSe, $CaF_2$, and $BaF_2$ have lower refractive indices and higher dispersion. More critically, they are incompatible with CMOS processes, making them unsuitable for use in LWIR metalens [32,37]. In contrast, Si and Ge, with their higher refractive indices and compatibility with CMOS processes, are the materials of choice for the reported LWIR metalens. However, Si exhibits strong absorption in the LWIR range, which is why traditional LWIR refractive lenses have been designed and fabricated primarily using Ge. Additionally, the synthesis of germanium is costly, and classical refractive lenses made from germanium are temperature-sensitive due to thermo-optic focal shift [38]. Nonetheless, the high synthesis cost of germanium and the temperature sensitivity of conventional refractive lenses due to thermo-optic focal shift

have somewhat limited its applications. In comparison, chalcogenide glasses have become the preferred choice for fabricating athermalized conventional refractive LWIR lenses due to their lower cost, excellent infrared transparency, and favorable thermo-optic properties. The previously criticized issue of mechanical fragility in chalcogenide glasses has also seen significant improvement with ongoing research and advancements in materials science. Currently, on-chip devices based on chalcogenide glass materials, such as waveguides, microrings, and microdisks, have demonstrated various functionalities including four-wave mixing, optical frequency comb generation, and ultrasound detection [38–41]. Furthermore, the advantages of CMOS-compatible processing, coupled with advancements in novel micro-nano fabrication technologies such as laser direct writing, 3D printing, and nanoimprinting, are poised to bring new development and application opportunities for chalcogenide glass-based infrared on-chip devices [19,42–44]. Given the current state of research, this paper reports on the design of single-wavelength and broadband achromatic LWIR metalenses using chalcogenide glass.

## 2. Materials and Methods

Figure 1 shows the schematic diagram of an all-chalcogenide single-wavelength (10 μm) non-achromatic and broadband (9.5–10.5 μm) achromatic metalens. Both metalenses' substrates and meta-atoms are made of the same chalcogenide glass, $As_2Se_3$, a commercially utilized chalcogenide glass material (Guangzhou, China). The glass, with excellent infrared transmittance, relatively flat dispersion, small thermo-optic coefficient, and low fabrication cost, has become the preferred material for making athermal traditional infrared lenses (for detailed parameters, please refer to the Supplementary Information). Considering the low energy of LWIR photons, we used radially symmetric cylindrical structures as meta-atoms in the design of single-wavelength non-achromatic metalens, which maximizes the utilization of incident light and enhances focusing efficiency, making the metalens polarization-insensitive. In contrast, to achieve broadband achromatic functionality, the meta-atoms of the achromatic metalens are designed as rectangular structures with varying heights, offering flexible design through multidimensional tuning.

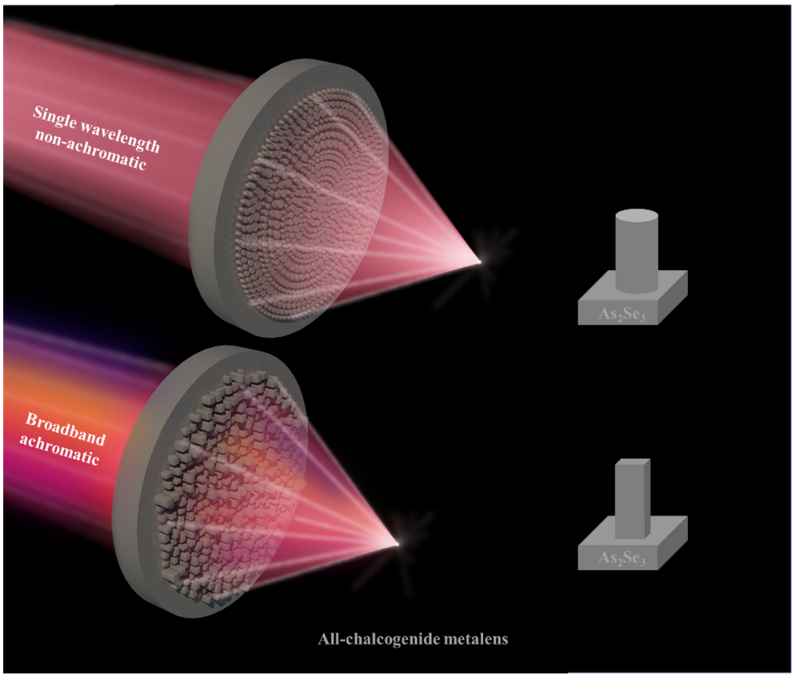



**Figure 1.** Schematic diagram of an all-chalcogenide single-wavelength (10 μm) non-achromatic and broadband (9.5–10.5 μm) achromatic metalens.

### *2.1. Single-Wavelength Non-Achromatic Metalens*

Principle

To design a metasurface functioning as a phase mask in transmission mode, we must create a set of unit cell structures with identical periods but varying dimensions. For high-efficiency wavefront modulation, these nanopillars should provide high transmittance and cover the entire 2π phase range. For a single-wavelength planar incident wave passing through the designed all-chalcogenide metalens to achieve wavefront convergence, the phase φ(r) that the nanopillar at position r(x, y) on the metalens need to provide is expressed as follows:

$$\varphi(r,\lambda) = -\frac{2\pi}{\lambda}\left(\sqrt{r^2+f^2}\right) - C(r_0,\lambda) \quad (1)$$

where $r = \sqrt{x^2+y^2}$ is the distance from arbitrary position (x, y) on the metalens to the center, λ represents the target wavelength in free space and f denotes the focal length. $C(r_0,\lambda) = -\frac{2\pi}{\lambda}\left(\sqrt{r_0^2+f^2}\right)$, which denotes the phase at the reference position $r_0 = \sqrt{x_0^2+y_0^2}$, is typically used to represent the phase at the lens center $r_0 = 0$ for simplicity and clarity in single-wavelength metalens design. Thus, Equation (1) can be expressed in a form that is commonly found in previous studies:

$$\varphi(r,\lambda) = -\frac{2\pi}{\lambda}\left(\sqrt{r^2+f^2}-f\right) \quad (2)$$

In this work, the metalens has a radius R of 100 μm and a focal length f of 50 μm. According to the numerical aperture (NA) calculation formula, $NA = n_0 \cdot R/(R^2+f^2)^{1/2}$, the NA of this metalens is as high as 0.89. Considering that the working wavelength is 10 μm and the metasurface is designed using an isolated cylindrical waveguide model, the height of the nanopillars should be comparable to the wavelength.

### *2.2. Broadband Achromatic Metalens*

Principle

Compared to broadband achromatic metalens, the single-wavelength metalens mentioned above exhibits pronounced chromatic aberrations. This is primarily due to the resonant phase dispersion of the meta-atoms used in the metalens, the intrinsic dispersion of the matrix material, and the varying phase accumulation of light at different wavelengths as it propagates through free space. Owing to the dispersion, metalenses generally display anomalous dispersion ($df/d\lambda > 0$), where longer working wavelengths correspond to shorter focal lengths, as illustrated in Figure 2a,b, contrasting sharply with the behavior of traditional geometric lenses [45]. To design a fixed-focal-length achromatic metalens, as schematically depicted in the lower part of Figure 1, it is essential to achieve consistent phase retardation in a wide range of wavelengths, as specified by Equation (1). Assuming the working wavelength is $\lambda \in [\lambda_{min}, \lambda_{max}]$, with $\lambda_{min}$ and $\lambda_{max}$ representing the boundaries the working wavelengths, Equation (1) can be reformulated as:

$$\varphi(r,\lambda) = \varphi_0(r,\lambda_{max}) + \Delta\varphi(r,\lambda) \quad (3)$$

with

$$\Delta\varphi(r,\lambda) = -2\pi\left(\sqrt{r^2+f^2}-\sqrt{r_0^2+f^2}\right)\left(\frac{1}{\lambda}-\frac{1}{\lambda_{max}}\right) \quad (4)$$

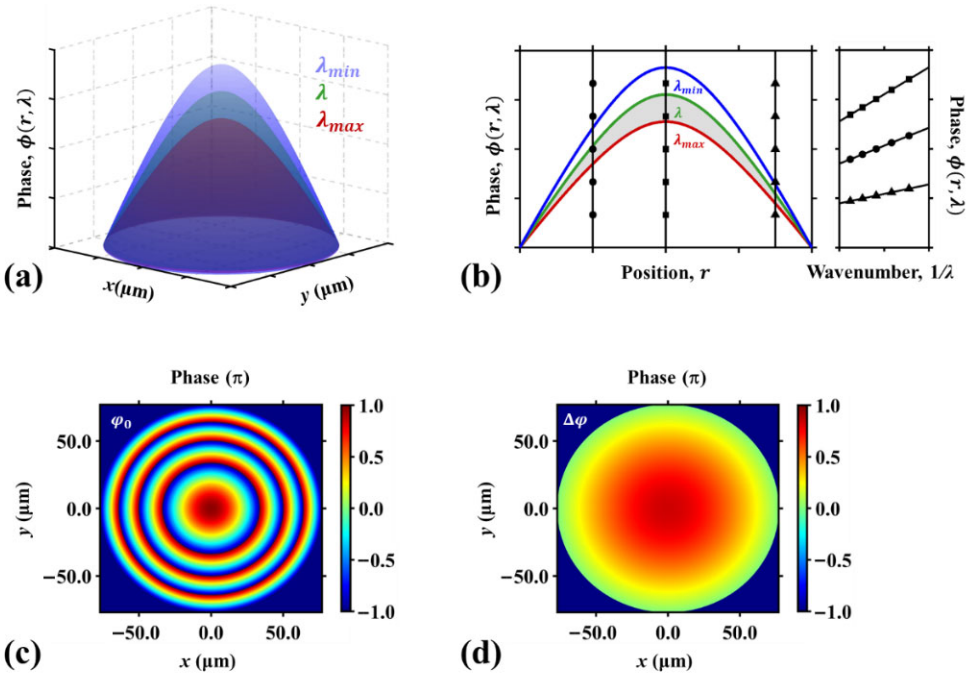



**Figure 2.** (**a**) Spatial phase distributions required for the designed achromatic metalens at various wavelengths. (**b**) Phase distribution of the achromatic metalens at different wavelengths (**left**), and the linear relationship between phase and wavenumber (1/λ) at three randomly selected positions (**right**). (**c**) Phase distribution of the designed achromatic all-chalcogenide metalens at λmax (10.5 μm). (**d**) Phase difference between the maximum (10.5 μm) and minimum (9.5 μm) wavelengths for the designed all-chalcogenide achromatic metalens.

As we can see, Equation (3) consists of two parts, with the former part $\varphi_0(r,\lambda_{max})$ depending solely on the maximum working wavelength $\lambda_{max}$ and representing its phase distribution. The latter part $\Delta\varphi(r,\lambda)$ is a function of the operating wavelength λ. As the metalens has a shorter f at longer wavelengths, as shown in left panel of Figure 2b, additional phase must be added to the longer wavelengths to match the f of shorter wavelengths, thereby correcting chromatic aberration between the two wavelengths. Thus, the $\Delta\varphi(r, \lambda)$ effectively represents the additional phase, which corresponds to the phase difference between long and short wavelengths. To ensure that $\Delta\varphi(r, \lambda)$ remains positive, it is necessary to satisfy $r_0 \geq r$, given that λmax is inherently greater than λ. In contrast to single-wavelength metalens designs where $r_0 = 0$, achromatic metalens typically uses $r_0 = R$, with the edge of the metalens as the reference point. Therefore, Equation (4) can be rewritten as follows:

$$\Delta\varphi(r,\lambda) = -2\pi\left(\sqrt{r^2+f^2} - \sqrt{R^2+f^2}\right)\left(\frac{1}{\lambda} - \frac{1}{\lambda_{max}}\right) \quad (5)$$

Moreover, $\Delta\varphi(r, \lambda)$ exhibits a strict linear dependence on the wavenumber 1/λ. This characteristic simplifies the broadband phase-matching problem to the dispersion compensation of the phase difference at the boundary wavelengths, thereby ensuring that chromatic aberration is fully corrected across the entire spectral range. The right panel of Figure 2b depicts the linear relationship between $\Delta\varphi(r, \lambda)$ and 1/λ at three different positions for the achromatic metalens. The varying slopes represent the phase gradient of the metalens, which is a function of r. This study pre-designs an achromatic metalens with a radius of R = 77 μm and a focal length of f = 50 μm for the 9.5–10.5 μm wavelength range. Figure 2c,d illustrate the phase distribution $\varphi_0$ and the phase compensation Δφ required for the maximum wavelength of $\lambda_{max}$ = 10.5 μm, respectively.

The next challenge in designing this broadband achromatic metalens is to engineer specialized meta-atoms that can correct the phase differences at the corresponding positions. To this end, we adopt the design approach used in the aforementioned all-chalcogenide metalens, constructing the meta-atoms using the dielectric waveguide-like transmission modes. The metalens can be modeled as a flat plate with a fixed thickness H and a spatially varying effective refractive index neff when reflection is neglected and only the phase of the transmitted light is considered. Under this condition, the transmission phase can be approximated as:

$$\varphi(r,\lambda) = \frac{2\pi}{\lambda} n_{eff}(r,\lambda) H \tag{6}$$

Accordingly, Equation (5) can be expressed as:

$$\varphi(r,\lambda) = \varphi_0(r,\lambda_{max}) + \Delta\varphi(r,\lambda) \tag{7}$$

With

$$\Delta\varphi(r,\lambda) = 2\pi H\left(\frac{n_{eff}(r,\lambda)}{\lambda} - \frac{n_{eff}(r,\lambda_{max})}{\lambda_{max}}\right) \tag{8}$$

As noted earlier, $\varphi_0(r, \lambda_{max})$ represents the phase distribution at the maximum wavelength, while $\Delta\varphi(r, \lambda)$ is the additional phase that ensures dispersion compensation. Both are closely linked to neff, which, according to the effective medium theory (EMT), is directly affected by the physical parameters of the meta-atoms, including their nanostructural shape, size, duty cycle, and lattice periodicity.

## 3. Results

### *3.1. Simulation of a Single-Wavelength Non-Achromatic Metalens*

#### 3.1.1. Simulation of Unit Structure

To achieve complete 2π phase coverage and high transmittance, this study employed the finite-difference time-domain (FDTD, the 2020 version) method. Under the conditions of periodic boundary conditions in the x and y directions and perfectly matched layers in the z direction, a parametric scan of the phase and transmittance was performed for nanopillars arranged in an infinitely periodic array on a substrate. Under plane-wave illumination, the simulation adopted an automatic convergence stop criterion, and the optimal height of the nanopillars was ultimately determined to be 13 μm. Subsequently, we simulated the phase and transmittance maps of the nanopillars as functions of the pillar diameter r and periods P, as illustrated in Figure 3b,c. It is evident that for certain specific values of the P, varying the radius of the nanocylinders can achieve entire 2π phase coverage while maintaining high transmittance. Considering the robustness of larger dimensions for practical fabrication equipment, we selected a periods P = 3.5 μm (The x-span and y-span of the FDTD simulation are both 3.5 μm, with a mesh accuracy of 2), as indicated by the white dashed lines. At this value, the phase covers an entire 2π range when the nanocylinder radius r varies from 0.95 μm to 1.53 μm, and the transmittance T remains high, reaching a maximum value of 1, as shown in Figure 3d. The high transmittance is primarily due to using the same material for both the substrate and the nanocylinder array, which avoids back reflection caused by impedance mismatch at the interface [46]. Furthermore, this value (P = 3.5 μm) also satisfies the Nyquist sampling theorem for spatial phase, $P < \lambda/(2NA)$.

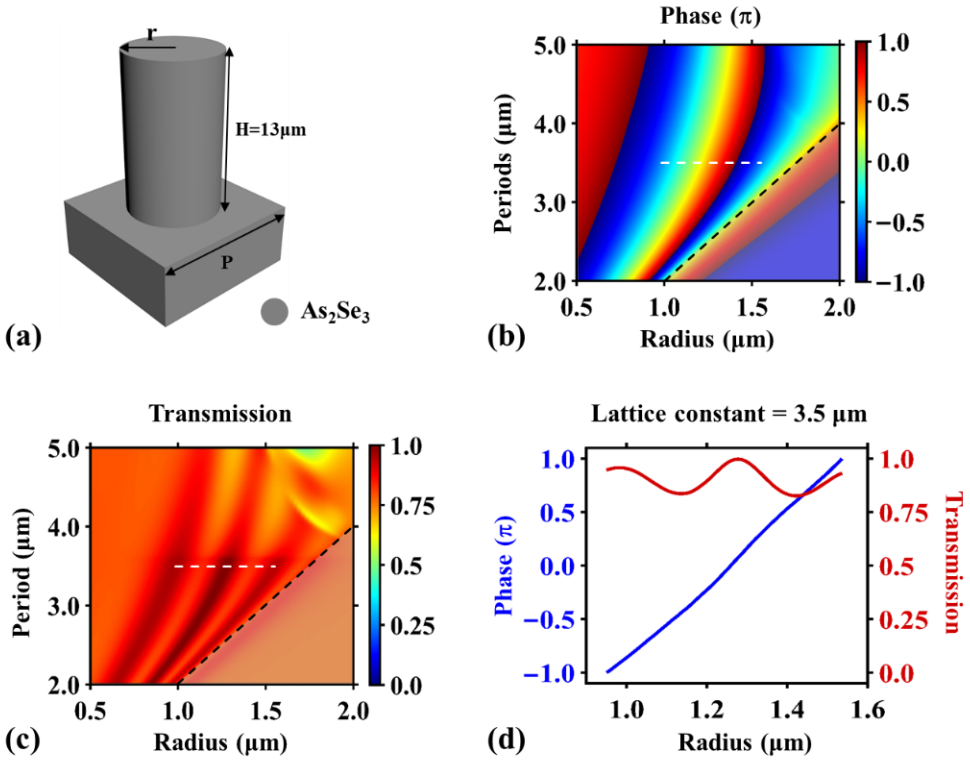



**Figure 3.** (**a**) Schematic diagram of the meta-atom of the all-chalcogenide metalens operating at 10 μm. (**b**) The phase corresponding to meta-atoms with different radii and periods. (**c**) The transmission corresponding to meta-atoms with different radii and periods. (**d**) Phase (blue line) and transmittance (red line) as functions of the nanocylinder (NP) radius, with a height (H) of 13 μm and period (P) of 3.5 μm.

### 3.1.2. Full Lens Simulation and Characterization

Based on the above parameters, we successfully constructed an all-chalcogenide long-wavelength infrared metalens with a radius of 100 μm and a focal length of 50 μm, as shown in Figure 4a. It is worth noting that for a perfect metalens, which can focus a normally incident plane wave to a diffraction-limited spot on the focal plane, its theoretical phase distribution is represented by the φ(x, y) equation mentioned above. It should be noted that the x and y here are considered infinite, meaning that, in an ideal scenario, the radius of the metalens would be infinitely large. However, when we define a finite radius for the metalens, its actual phase distribution deviates from the theoretical one, as shown in Figure 4b,c below. This discrepancy leads to the numerical aperture (NA) of the practical metalens being consistently smaller than that of an ideal, infinitely large metalens. To better observe this difference, we extracted and compared the phase at the position of the white dashed line (y = 0 μm) in the figure, as shown in Figure 4d. The black dashed line illustrates the theoretical phase as a function of position along the x-axis, while the blue solid line shows the actual phase. Discrete red circles correspond to nanopillars of varying radii, positioned along the x-axis according to the target phase indicated by the black dashed line. Close to the center of the metalens, the theoretical and actual phases exhibit a strong alignment. However, as the distance from the center increases, the discrepancy between the two phases progressively widens. This discrepancy arises partly from the finite size of the practical metalens as previously mentioned, and partly from the increasing phase gradient away from the lens center. The primary cause of latter issue is the pronounced variation in radius between adjacent nanopillars, which deviates from the gradual phase changes typically employed in conventional forward design. Moreover, the unit cell design utilizes periodic boundary conditions and does not account for the direct coupling between adjacent

nanopillars, thereby exacerbating the discrepancy between the actual and theoretical phases. This discrepancy between theoretical and actual wavefront phases not only reduces the NA of the metalens but also becomes apparent in the focal length and spot size, as elaborated in the subsequent sections.

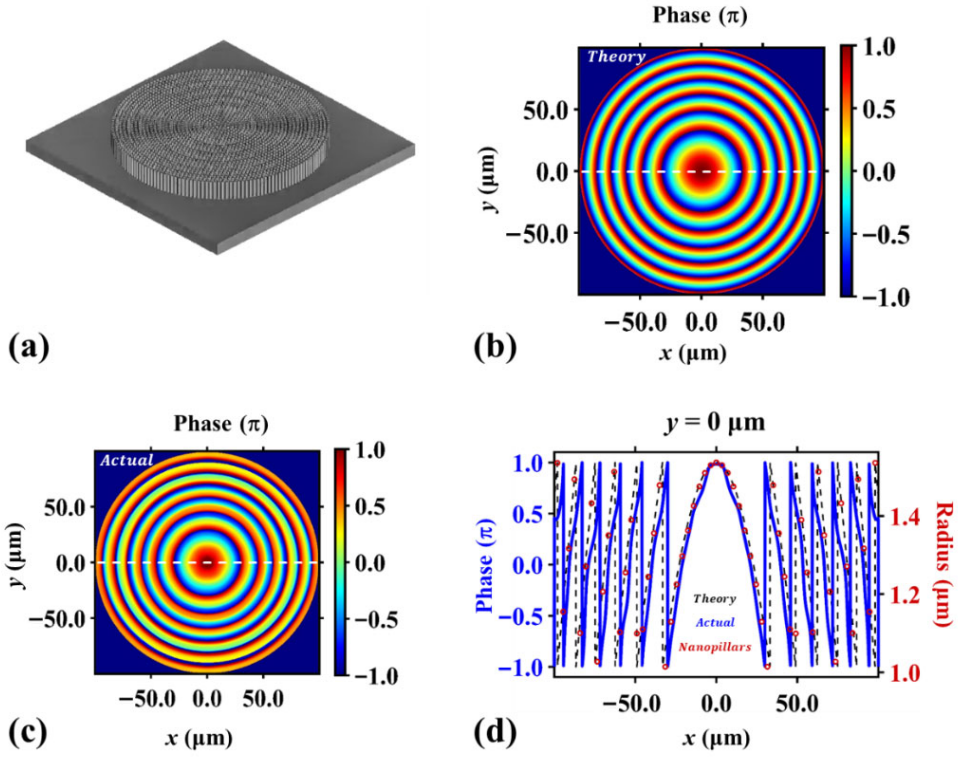



**Figure 4.** (**a**) Simulated model of the all-chalcogenide LWIR metalens with a radius of 100 μm and a focal length of 50 μm. (**b**) Theoretical phase distribution of the all-chalcogenide metalens operating at 10 μm. (**c**) Actual phase distribution of the all-chalcogenide metalens constructed to operate at 10 μm. (**d**) Theoretical and actual phase distributions of the all-chalcogenide metalens along the x-axis at y = 0, with corresponding nanostructure radii at each position.

Figure 5a illustrates the normalized intensity distribution in the xz propagation plane, with the peak intensity occurring at 47.3 μm, as marked by the white dashed line, which has a slight deviation from the theoretical focal length (f = 50 μm). The focal length deviation is caused by the aforementioned discrepancy between the theoretical and actual phase distributions. To minimize these issues, additional algorithms are required to refine the metalens's structural parameters, a process that will be detailed in the following discussion on achromatic metalens design. Figure 5b presents the normalized 2D intensity distribution along the white dashed line. The focal spot in the focal plane exhibits a slight elliptical distribution. To more clearly illustrate the characteristics of the focal spot, the intensity distributions along the x and y axes are depicted by blue and red solid lines, respectively. A slight difference in the focal spot size between the x and y directions can be observed from the variations in the full width at half maximum (FWHM) of the blue and red intensity profiles. This discrepancy may be attributed not only to the previously mentioned theoretical and actual phase errors but also, more likely, to the linearly polarized incident light being x-polarized. For the latter, this is a common issue under the tight focusing conditions of high Numerical aperture (NA > 0.7) lenses, which can be numerically explained using vectorial Debye theory [47]. This issue similarly arises in the high-NA achromatic metalens focusing discussed in subsequent sections. Additionally, the intensity distribution curves along the x and y axes show that the maximum side lobe intensity is

less than 3% of the central intensity, suggesting that the side lobes have a negligible impact on the metalens's field of view.

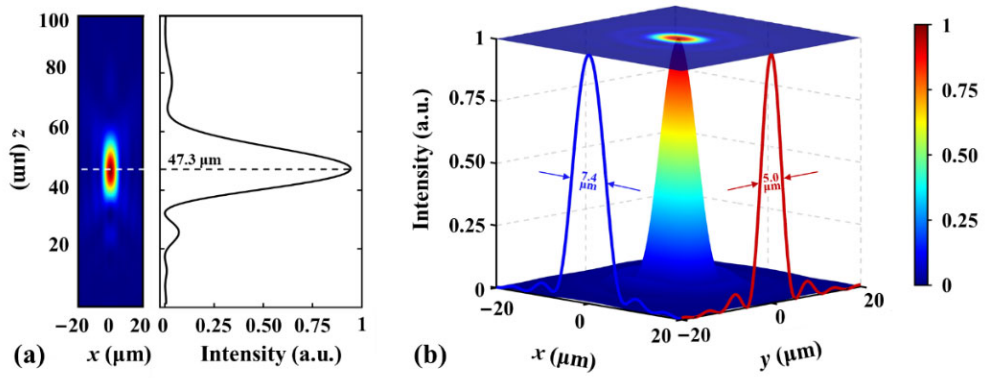



**Figure 5.** (**a**) Normalized intensity distribution of the designed all-chalcogenide metalens in the xz propagation plane, with the actual focal length marked by the white dashed line. (**b**) Normalized intensity distribution at the focal plane.

### *3.2. Simulation of Broadband Achromatic Metalens*

#### 3.2.1. Simulation of Unit Structure

We first select the same meta-atoms used in the aforementioned single-wavelength metalens nanopillars, as shown in Figure 6a. To broaden the tuning range of neff and ensure that the required phase φ(r, λ) can be achieved at every position on the metalens, both the radius r and height h of the chalcogenide nanopillars are treated as variable parameters, while keeping the overall height H constant. Although this approach undoubtedly adds fabrication challenges, advances in micro- and nanofabrication techniques, such as 3D printing, two-photon polymerization, laser processing, and nanoimprint lithography, have made the production of variable-height metalens feasible. Each meta-atom with a specific neff provides a set of ($\varphi_0$, Δφ) values, and the discrete ($\varphi_0$, Δφ) points from thousands of different meta-atoms span a region in the $\varphi_0$-Δφ space, as illustrated by the blue region in Figure 6b. In the figure, the orange dots represent the required ($\varphi_0$, Δφ) values at each position on the metalens. A larger blue region corresponds to greater coverage of the orange dots, indicating that the meta-atoms can more precisely match the required ($\varphi_0$, Δφ) at each position on the metalens. The meta-atom in the blue region that has the shortest Euclidean distance to each orange dot will be chosen for constructing the metalens, if the blue region does not fully cover the orange dots. Clearly, a larger blue coverage area facilitates the selection of meta-atoms with the closest ($\varphi_0$, Δφ) match, bringing the designed metalens closer to the theoretical model and significantly enhancing its performance, including focal length f and focusing efficiency. However, despite the flexibility afforded by adjusting the r, h and P of the nanopillars, the ($\varphi_0$, Δφ) range provided by this meta-atom library remains inadequate, with many orange dots falling outside its coverage area, as illustrated in Figure 6b. More complex nanopillars, such as annular or concentric pillars, can increase the dimensionality of adjustment, thereby enriching the meta-atom library and expanding the ($\varphi_0$, Δφ) coverage range. However, greater complexity and higher aspect ratios inevitably exacerbate fabrication challenges. To address this, a simple nanobrick with enhanced control dimensions is used to build the meta-atom library for the metalens, as shown in Figure 6c. Utilizing these nanobricks, which can be tuned in dimensions such as length L, width W, height h, and period P, the meta-atom library offers an expanded ($\varphi_0$, Δφ) coverage range, nearly covering all the orange dots, as illustrated in Figure 6d. The few remaining uncovered orange dots are in close proximity to the blue region, with only a small distance separating them. This suggests that the nanobrick meta-atom library can

provide adequate matching units for constructing achromatic metalenses at both the $\lambda_{max}$ (10.5 μm) and $\lambda_{min}$ (9.5 μm) discrete wavelengths. Additionally, the transmittance of all the nanobricks is consistently 0.79, ensuring that the metalens maintains a relatively high focusing efficiency. However, achieving chromatic correction for continuous wavelengths within the ($\lambda_{min}$, $\lambda_{max}$) range still depends on the linearity of $\Delta\varphi$ with respect to $1/\lambda$.

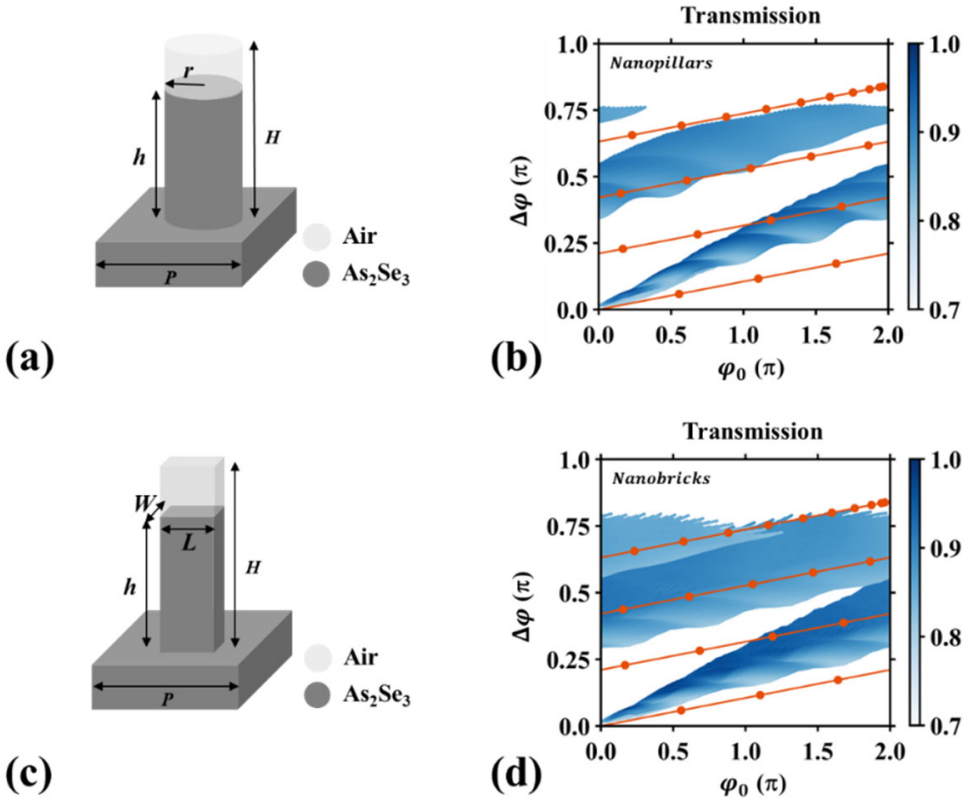



**Figure 6.** (**a**) Schematic of the preset nanopillar meta-atom used in the construction of the all-chalcogenide achromatic metalens. (**b**) Calculated phase $\varphi_0$ at the maximum wavelength and additional phase $\Delta\varphi$ for each nanopillar in the meta-atom library constructed using nanopillars in the 9.5–10.5 μm wavelength range. (**c**) Schematic of the preset nanobrick meta-atom used in the construction of the all-chalcogenide achromatic metalens. (**d**) Calculated phase $\varphi_0$ at the maximum wavelength and additional phase $\Delta\varphi$ for each nanobrick in the meta-atom library constructed using nanobricks in the 9.5–10.5 μm wavelength range. The orange dots represent the required ($\varphi_0$, $\Delta\varphi$) values at each position on the metalens. The color scale indicates the transmittance, with higher values corresponding to increased transmission efficiency.

To validate chromatic correction across a continuous wavelength range from $\lambda_{min}$ to $\lambda_{max}$, we randomly selected four nanobrick structures with different L, W, and h, and analyzed their phase and transmittance, as shown in Figure 7. It can be observed that the phase $\varphi$ provided by all nanobricks with varying parameters (L, W, h) exhibits strong monotonicity and linearity across the entire 9.5–10.5 μm range (as shown by the blue curves), ensuring that the metalens constructed from these meta-atoms can achieve achromatic performance throughout the wavelength range. Furthermore, as noted earlier, all nanobricks exhibit high transmittance across the 9.5–10.5 μm range, ensuring that the metalens maintains high transmission efficiency.

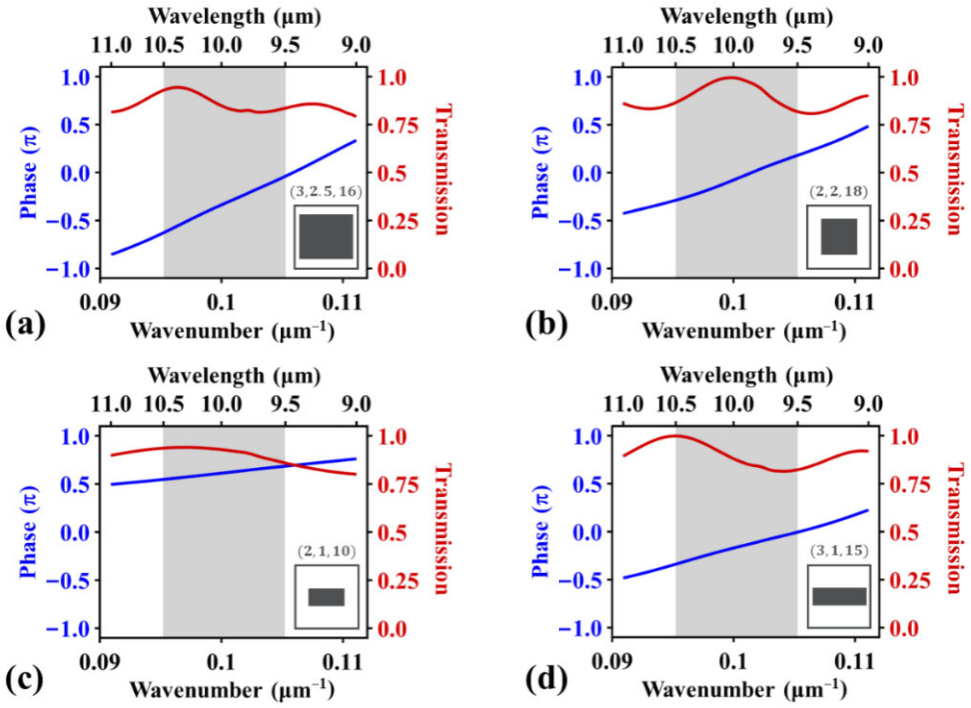



**Figure 7.** The phase and transmittance corresponding to nanobricks with varying lengths (L), widths (W), and heights (h) were calculated. (**a**) Nanobrick with size parameters (3, 2.5, 16); (**b**) nanobrick with size parameters (2, 2, 18); (**c**) nanobrick with size parameters (2, 1, 10); (**d**) nanobrick with size parameters (3, 1, 15).

### 3.2.2. Full Lens Simulation and Characterization

To prevent the issues seen in single-wavelength metalens, such as phase discontinuities and coupling between adjacent unit structures that lead to deviations between actual and theoretical phase distributions, impacting f, spot size, and focusing efficiency, we introduced a particle swarm optimization (PSO) algorithm in the design of the broadband achromatic metalens to minimize these effects and improve its overall performance. The particle swarm optimization algorithm was first proposed by Kennedy and Eberhart in 1995 as a swarm intelligence algorithm that simulates the cooperation and information sharing behavior among individuals in a bird flock during foraging [48]. The core advantage of PSO lies in its independence from gradient information of the objective function, making it widely applicable to complex optimization scenarios characterized by nonlinearity, non-differentiability, multimodality, and noise [49]. Given the sensitivity of PSO to initial parameters, selecting appropriate initialization values can significantly reduce computational costs and improve the likelihood of finding an optimal global solution. To achieve this, we performed iterative optimization using the conventional finite-difference time-domain (FDTD) method, with the complete optimization process illustrated in Figure 8, where the number of particles is 40 and the number of iterations is 300. To reduce focal length deviation and enhance focusing efficiency, we define the figure of merit (FOM) as follows:

$$\mathrm{FOM} = \sum_{i=1}^{n} \left( a \frac{|f_a(\lambda_i) - f|}{f} + b \frac{1}{I(\lambda_i)} \right) \quad (9)$$

In the formula, $f_a(\lambda_i)$ represents the measured focal length at the i-th wavelength; f is the theoretical focal length; and $I(\lambda_i)$ is the peak intensity at the theoretical focal position for the i-th wavelength. This Figure of Merit (FoM) consists of two components: the first term represents the focal length error rate, which quantifies the relative deviation between the measured focal length and the theoretical value; the second term is the reciprocal of $I(\lambda_i)$,

used to evaluate the focusing efficiency. Since there is no significant conflict between the two objectives, they can be converted into a single objective by assigning weight coefficients, and the optimization focus can be flexibly adjusted by tuning a and b (with a = 1 and b = 1 as a possible initial choice for the weights). Considering the inherent correlation between the peak intensity and the focal plane position (the position of maximum intensity is typically defined as the measured focal length), the FoM can be further reformulated as follows to reduce computational complexity and improve optimization efficiency:

$$\mathrm{FOM} = \sum_{i=1}^{n}\left(a\frac{|I_a(\lambda_i) - I(\lambda_i)|}{I(\lambda_i)} + b\frac{1}{I(\lambda_i)}\right) \tag{10}$$

Here, $I_a(\lambda_i)$ represents the peak intensity at the measured focal length for the i-th wavelength. Clearly, this FoM is a reverse indicator: the smaller its value, the smaller the focal length deviation and the higher the focusing efficiency, thereby providing an optimization direction for improving the performance of achromatic metalenses. The particle velocity update formula based on the particle swarm optimization algorithm is as follows:

$$v_{t+1} = \omega v_t + c_g r_1 (gbest_t - x_t) + c_p r_2 (pbest_t - x_t) \tag{11}$$

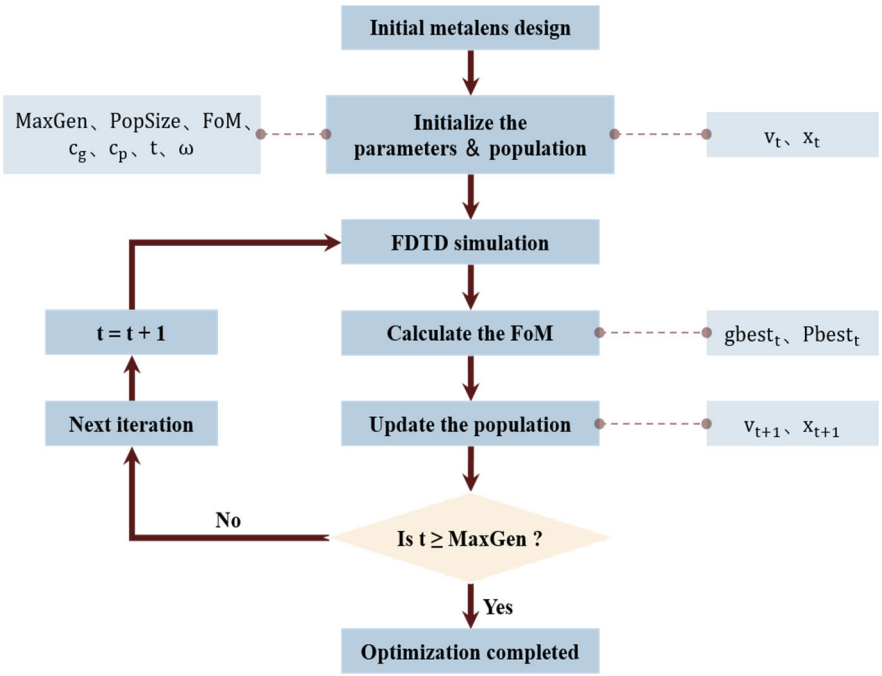



**Figure 8.** Design process for broadband achromatic metalens optimization using PSO algorithm. MaxGen denotes the maximum number of iterations; PopSize represents the population size; FoM is the figure of merit; $c_g$ and $c_p$ represent the global learning factor and the individual learning factor, respectively; t is the iteration counter; ω is the inertia coefficient; $v_t$ and $x_t$ denote the velocity and position of an individual in the current generation, while $v_{t+1}$ and $x_{t+1}$ are the velocity and position of an individual in the next generation; $gbest_t$ and $pbest_t$ are the global best solution and the individual best solution, respectively.

Among them, $r_1$ and $r_2$ are random numbers in the interval [0, 1], used to enhance the flexibility of particle search. From a physical perspective, the particle velocity update is influenced by the combined effect of three components: the first term is the inertia component (also known as the inherent cognition term), which reflects the particle's tendency to maintain its original motion state; the second term is the social component (collective cognition term), which guides the particle toward the global best position found

by the swarm; the third term is the individual component (self-cognition term), which drives the particle toward its own personal best position.

The optimized all-chalcogenide broadband achromatic LWIR metalens is shown in Figure 9a, with its spatial focusing performance demonstrated in Figure 9b. For clearer and more intuitive visualization of the focusing performance, the intensity distributions at different operating wavelengths are shown in the propagation plane containing the optical axis (xz-plane at y = 0) and the focal plane (xy-plane at z = z($f_{actual}$)), respectively, as depicted in the left and right panels of Figure 9c. It can be observed that the metalens maintains an almost constant f across the 9.5–10.5 μm wavelength range, demonstrating outstanding achromatic performance. Moreover, the point spread function (PSF) at the focal point maintains a high degree of symmetry, with the focal spots at each wavelength approaching the diffraction limit, indicating minimal aberrations. These characteristics are further confirmed by the intensity distributions along the z-axis cross-section and at the focal point (in the xy-plane), as shown in Figure 9d. In stark contrast to the single-wavelength metalens designed without the PSO algorithm, the intensity distribution curves along the x and y axes in the focal plane of the achromatic metalens nearly overlap, underscoring the PSO algorithm's effectiveness in reducing the deviation between the actual and theoretical phase distributions. Moreover, the reduction in the maximum sidelobe intensity relative to the central intensity further enhances the focusing efficiency of the metalens.

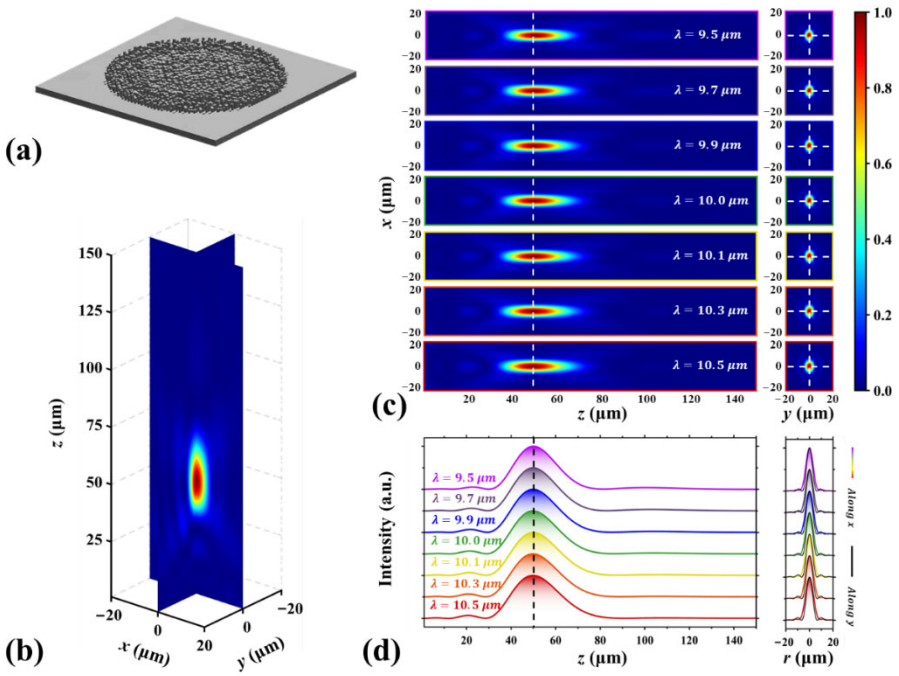



**Figure 9.** (**a**) The simulation model for the designed all-chalcogenide LWIR achromatic metalens. (**b**) The 3D spatial distribution of focal intensity for the designed achromatic metalens. (**c**) The intensity distribution at different operating wavelengths of the propagation plane (xz plane at y = 0, (**left**)) and the focal plane (xy plane at z = z($f_{actual}$), (**right**)). (**d**) Focal spot intensity distribution curves at different wavelengths along the propagation direction (**left**) and in the focal plane (**right**).

To further assess the performance of the achromatic metalens, we extracted and meticulously analyzed the focal length, focusing efficiency, and full width at half maximum (FWHM) of the planar intensity distribution across seven wavelengths within the operational range. To assess the impact of the PSO algorithm, we compared the performance of a broadband achromatic metalens in the 9.5–10.5 μm range, also constructed using nanobricks, but without PSO. Additionally, the performance of a single-wavelength non-achromatic metalens designed for 10 μm, also constructed us-

ing nanobricks, was compared. Figure 10a shows the focal lengths of the three metalenses across the 9.5–10.5 μm operating range. It is clear that the non-achromatic metalens, designed for operation at a single wavelength of 10 μm, shows a substantial deviation between the $f_{actual}$ and $f_{theory}$ ($\Delta f = |(f_{actual} - f_{theory})/f_{theory}|$) of approximately 7.6%. Across the 9.5–10.5 μm range, the factual varies from 51.1 μm to 42.4 μm, with an average focal length ($\overline{f_{actual}} = \sum f_{actual}/N$) of 46.5 μm and an average focal length error ($\overline{\Delta f} = \left(\overline{f_{actual}} - f_{theory}\right)/f_{theory}$) of 7%. In contrast, despite not being optimized with the PSO algorithm, the achromatic metalens shows a focal length variation of 47.2 μm to 48.5 μm within the 9.5–10.5 μm range, with a $\overline{f_{actual}}$ of 48 μm and a $\overline{\Delta f}$ to approximately 3.9%. As anticipated, the PSO-optimized achromatic metalens shows a significantly smaller focal length variation, ranging from 49.8 μm to 50 μm, with a $\overline{f_{actual}}$ of 49.9 μm and a $\overline{\Delta f}$ of just 0.1%, demonstrating outstanding dispersion control and focal length accuracy. Figure 10b illustrates the full width at half maximum (FWHM) of the focal spot intensity distributions along the x-axis (triangles) and y-axis (circles) for the three metalenses at various working wavelengths, with the theoretical diffraction limit shown by the black dashed line. Although the FOM in our PSO algorithm was not specifically optimized for this metric, the PSO-optimized metalens exhibits a smaller FWHM difference along the x and y axes compared to both the single-wavelength non-achromatic and non-PSO-optimized achromatic metalenses, indicating superior circular symmetry of the focal spot, as confirmed in Figure 9. The origin of this deviation was previously discussed in the analysis of the single-wavelength metalens, attributed to the mismatch between the actual and theoretical phase distributions of the metalens and the polarization characteristics of the incident light. We anticipate that future metalens designs will see a substantial enhancement in focusing performance if the FWHM of the intensity distribution along the x and y axes is incorporated into the FOM of the PSO algorithm. The focusing efficiency of a metalens is generally classified into absolute focusing efficiency (AFE) and relative focusing efficiency (RFE). AFE is usually defined as the ratio of the power within a circle of diameter 3 × FWHM at the focal spot to the total power incident on the metalens, although some studies use a diameter of 6 × FWHM for this measurement [50]. RFE, or diffraction efficiency, is generally defined as the ratio of the power within a circle of diameter 3 × FWHM at the focal spot to the total power transmitted through the metalens. The AFE and RFE of the three metalenses operating in the 9.5–10.5 μm range were calculated and are presented in Figures 10c and 10d, respectively. It is evident that the non-PSO-optimized achromatic metalens exhibits the lowest AFE and RFE, while the PSO-optimized version shows substantial improvement in both metrics, with the RFE in particular reaching levels comparable to those of the non-achromatic metalens. Since the total incident power remains constant and the AFE of the non-achromatic metalens exceeds that of the PSO-optimized achromatic metalens, this suggests that, according to the AFE definition, the optical power at the focal spot is greater for the non-achromatic metalens than for the PSO-optimized achromatic metalens. Meanwhile, given the similarity in RFE between the two metalenses, and considering both the focal spot intensity and the RFE definition, it can be inferred that the transmittance of the non-achromatic metalens is higher than that of the achromatic metalens. This phenomenon is likely attributed to the greater phase deviation between the achromatic metalens and the ideal phase distribution, compared to the smaller phase deviation in the single-wavelength non-achromatic metalens. As outlined in the theoretical design of the achromatic metalens and shown in Figure 5, achieving achromatic performance requires overlaying a non-uniform phase distribution $\Delta\varphi$ onto an ideal single-wavelength non-achromatic phase distribution $\varphi_0$. This modification disrupts the smooth phase transition and exacerbates phase discontinuities between adjacent meta-atoms. Additionally, for broadband achromatic metalenses, the relationship between $\Delta\varphi$ and $1/\lambda$ is not

perfectly linear across the operating wavelength range, as shown in Figure 7, which further contributes to the phase discontinuities between adjacent meta-atoms and the deviations from the theory phase distribution. These effects ultimately lead to greater transmission losses and reduced focal spot intensity in the achromatic metalens compared to the single-wavelength non-achromatic metalens. Fortunately, the performances of the achromatic metalens have been significantly improved through optimization with the PSO algorithm.

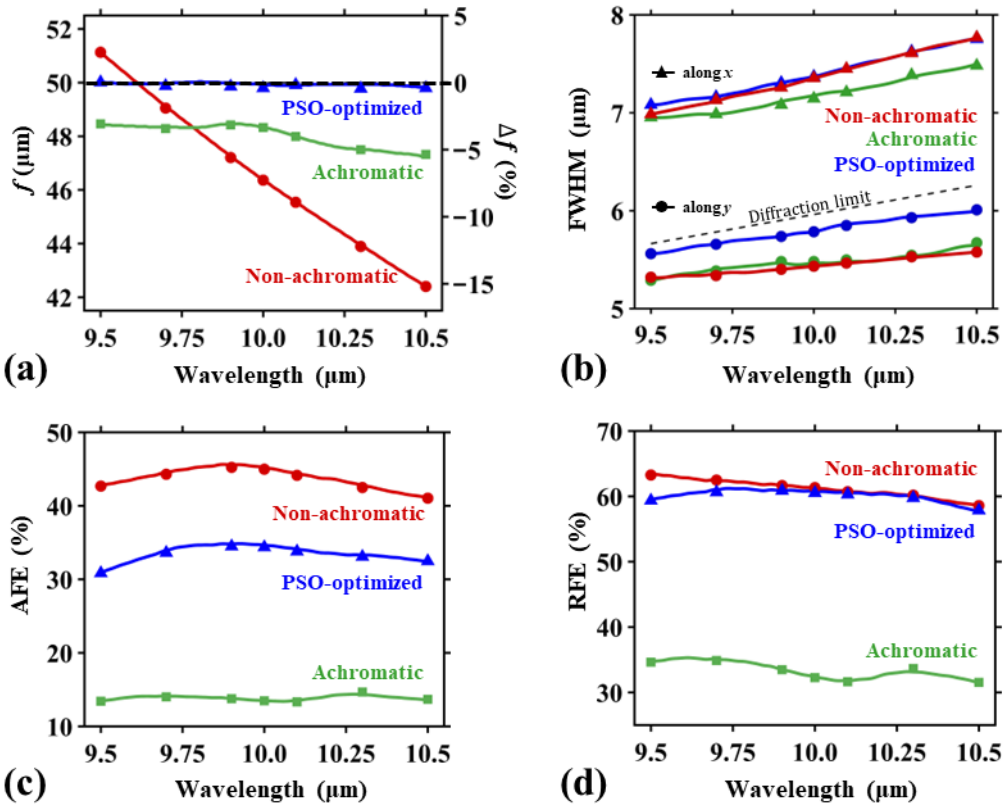
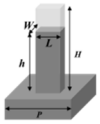
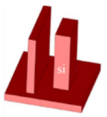
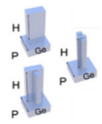
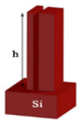
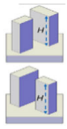
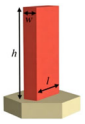



**Figure 10.** Focusing performance at different wavelengths for the single-wavelength non-achromatic metalens (red), unoptimized achromatic metalens (cyan), and PSO-optimized achromatic metalens (blue) based on the all-chalcogenide nanobrick library (**a**); full width at half maximum (FWHM) of intensity distributions along the x and y axes at the focal spot (**b**); absolute focusing efficiency (AFE) (**c**) and relative focusing efficiency (RFE) (**d**) of the three metalenses.

### 3.2.3. This Study Compares the Performance of Other Achromatic Metalenses in the Long-Wave Infrared Band

To the best of our knowledge, this represents the first realization of a broadband achromatic metalens using chalcogenide glass as an LWIR material. This metalens achieves performance optimization and functional integration through a single-layer metasurface, overcoming the limitations of conventional multilayer stacking approaches. In terms of performance optimization, the particle swarm optimization algorithm is innovatively employed for inverse design assistance. While maintaining a large numerical aperture (NA = 0.84), this approach achieves a significant improvement in focusing efficiency (33.2%) and a substantial reduction in focal length error (0.1%). Compared to previously reported LWIR achromatic metalenses based on Si or Ge, this design offers a higher numerical aperture, reduced focal length error, and relatively high focusing efficiency, as summarized in Table 1. Moreover, considering the lower cost of chalcogenide glass, along with its lower transmission loss and thermo-optic coefficient in the LWIR range compared to Si and Ge, the all-chalcogenide LWIR broadband achromatic metalens holds great promise for practical applications.

**Table 1.** Summary of reported long-wave infrared (LWIR) achromatic metalens performance.

| Parameter \ Reference | This Work | [51] | [35] | [52] | [50] | [3] |
|---|---|---|---|---|---|---|
| Patterns |  |  |  |  |  |  |
| Phase control | Propagation | Propagation | Propagation + PB | Propagation + PB | Propagation | Propagation + PB |
| Materials | $As_2Se_3$ | Si | Ge | Si | Si | Si |
| Wavelength (μm) | 9.5–10.5 | 8.6–11.4 | 9.6–11.6 | 8.6–11.4 | 8.5–11.5 | 9–11 |
| Diameter (μm) | 154 | 191.4 | 400 | 280 | 200 | 130.5 |
| Ambient medium | Air | Air | Air | Air | Air | Air |
| NA | 0.84 | 0.54 | 0.32 | 0.45 | 0.33 | 0.79 |
| $\lvert \Delta f \rvert$ (%) | 0.11 [a] | 5.88 [b] | - | 1.16 [c] | 8.8 [c] | 3.95 [c] |
| Def. (AFE) | 3 × FWHM | - | 6 × FWHM | - | 6 × FWHM | - |
| AFE (%) | 34 | 38.22 | 31 | 27.66 | 10 | 20.06 |
| Function | Focusing | Focusing | Focusing | Focusing | Focusing | Focusing |
| Exp. or Sim. | Sim. | Sim. | Sim. | Sim. | Exp. | Sim. |

-: Not given; [a] $|\Delta f| = \left(f_{actual} - f_{theory}\right)/f_{theory}$, [b] $|\Delta f| = \frac{f_{max} - f_{min}}{\bar{f}}$, [c] $|\Delta f| = \frac{f_{max} - f_{theory}}{f_{theory}}$.

## 4. Discussion

This study focuses on the design and development of a metalens based on all-chalcogenide materials. We design a broadband achromatic metalens operating in the long-wave infrared band. This device achieves a significant performance improvement over conventional designs, attaining a focusing efficiency of 33.2% and a focal length error of 0.1% while maintaining a large numerical aperture. Notably, this work reports for the first time a long-wave infrared broadband achromatic metalens based entirely on chalcogenide materials, employing a particle swarm optimization algorithm for inverse-assisted optimization. As a result, while preserving a large numerical aperture, the device achieves both a marked enhancement in focusing efficiency and a substantial reduction in focal length error. Although the broadband achromatic metalens in this study has achieved promising results in the simulation stage, several technical challenges may be encountered during fabrication. First, precise control is difficult to achieve: loading effects and etching lag lead to poor height uniformity, while high-aspect-ratio structures are prone to morphological defects such as sidewall roughness and undercutting. Moreover, the etching selectivity and damage control of chalcogenide glass limit process stability. Second, phase deviations caused by fabrication errors may compromise the achromatic performance of the metalens, resulting in focal length shift, reduced focusing efficiency, and numerical aperture degradation.

Accordingly, future work can be further explored in the following two directions:

1. Process optimization: Employ inductively coupled plasma (ICP) etching and sidewall passivation techniques to suppress undercutting and etching lag, thereby improving the precision of height control.

2. Process substitution: Adopt emerging techniques such as two-photon 3D printing and grayscale nanoimprint lithography to achieve both high precision in variable-height structures and efficiency in mass production.

Although the variable-height nanopillars of the achromatic metalens designed and developed in this study increase fabrication complexity to a certain extent, modern micro/nano-fabrication technologies have already provided technical guarantees for realizing such variable-height metalenses. The variable-height nanopillar metalens proposed in this study is expected to become a core component of next-generation lightweight and integrated optical systems, playing an important role in fields such as consumer electronics, biomedical engineering, optical communications, and autonomous driving.

## 5. Conclusions

This study proposes an innovative design scheme for a metalens based on chalcogenide glass materials, aiming to meet the growing application demands in the long-wave infrared (8–14 μm) band for fields such as thermal imaging, biomedicine, and intelligent driving. Using the commercial chalcogenide material $As_2Se_3$, we first designed a polarization-insensitive, all-chalcogenide, single-wavelength metalens operating at 10 μm with a large numerical aperture (NA = 0.89). Through a propagation-phase modulation approach, a measured focal length of 47.3 μm was achieved (target focal length: 50 μm), with the deviation attributed to phase distribution mismatch caused by the finite aperture size and the use of periodic boundary conditions. To further enhance device performance, we designed an all-chalcogenide broadband achromatic metalens operating in the 9.5–10.5 μm range with a large numerical aperture (NA = 0.84). By employing a particle swarm optimization algorithm for global optimization of the nanostructural parameters, a focal length deviation of only 0.1% and an average focusing efficiency as high as 34% were achieved. Compared to metalenses designed with conventional long-wave infrared materials, the all-chalcogenide metalens exhibits notable advantages, including a low thermo-optic coefficient, low transmission loss, and low cost. This provides a revolutionary solution for the miniaturization of long-wave infrared optical systems and wide-spectrum high-resolution imaging, holding broad application prospects in free-space communications, miniature spectrometers, and portable thermal sensing devices.

**Supplementary Materials:** The following supporting information can be downloaded at: https://www.mdpi.com/article/10.3390/photonics13050433/s1, Figure S1: The refractive index $n$ and extinction coefficient $k$ of chalcogenide glass $As_2Se_3$ in the infrared range of 8–12 μm, with the grey area indicating the operational bandwidth of the achromatic metalens designed in this study.

**Author Contributions:** Conceptualization, M.Z., Y.C., Z.H. and M.L.; methodology, M.Z., Y.C., Z.H. and M.L.; software, Z.H. and M.L.; validation, Z.H. and M.L.; formal analysis, M.Z., Y.C., Z.H. and M.L.; investigation, Z.H., M.L., Y.S., H.X. and Y.F.; resources, M.Z. and Y.C.; data curation, M.Z., Y.C., Z.H. and M.L.; writing—original draft preparation, M.Z., Y.C., Z.H. and M.L.; writing—review and editing, M.Z., Y.C., Z.H. and M.L.; supervision, M.Z., Y.C., Y.Z., S.Z. and Z.C.; project administration, M.Z., Y.C., Y.Z., S.Z. and Z.C.; funding acquisition, M.Z. and Y.C. All authors have read and agreed to the published version of the manuscript.

**Funding:** This work was supported in part by the Natural Science Foundation Project of Guangdong Province's Basic and Applied Basic Research Fund (2026A1515012016), National Natural Science Foundation of China (NSFC) (62005098, 61935013), General items of Guangzhou Science and Technology Plan Project (Ph.D. Young Scientists and Technologists category) (202201010320), and the Fundamental Research Funds for the Central University (11623415).

**Data Availability Statement:** Data underlying the results in this paper may be obtained from the authors upon reasonable request.

**Conflicts of Interest:** Author Yi Zhou was employed by the company Guangzhou Idealmeta Technology Co., Ltd. The remaining authors declare that the research was conducted in the absence of any commercial or financial relationships that could be construed as a potential conflict of interest.

## References

1. Kateb, B.; Yamamoto, V.; Yu, C.; Grundfest, W.; Gruen, J.P. Infrared Thermal Imaging: A Review of the Literature and Case Report. *NeuroImage* **2009**, *47*, T154–T162. [CrossRef]
2. Shakhatreh, H.; Sawalmeh, A.H.; Al-Fuqaha, A.; Dou, Z.; Almaita, E.; Khalil, I.; Othman, N.S.; Khreishah, A.; Guizani, M. Unmanned Aerial Vehicles (UAVs): A Survey on Civil Applications and Key Research Challenges. *IEEE Access* **2019**, *7*, 48572–48634. [CrossRef]
3. Zhao, L.-R.; Jiang, X.-Q.; Li, C.-X.; Gong, S.-X.; Yu, W.-X. High-NA and Broadband Achromatic Metalens for Sub-Diffraction Focusing of Long-Wavelength Infrared Waves. *Results Phys.* **2023**, *46*, 106308. [CrossRef]
4. Qi, J.; Sun, C.; Zebibula, A.; Zhang, H.; Kwok, R.T.K.; Zhao, X.; Xi, W.; Lam, J.W.Y.; Qian, J.; Tang, B.Z. Real-Time and High-Resolution Bioimaging with Bright Aggregation-Induced Emission Dots in Short-Wave Infrared Region. *Adv. Mater.* **2018**, *30*, 1706856. [CrossRef]
5. Wang, S.; Wu, P.C.; Su, V.-C.; Lai, Y.-C.; Chen, M.-K.; Kuo, H.Y.; Chen, B.H.; Chen, Y.H.; Huang, T.-T.; Wang, J.-H.; et al. A Broadband Achromatic Metalens in the Visible. *Nat. Nanotechnol.* **2018**, *13*, 227–232. [CrossRef]
6. Hao, J.; Ma, T.; Ye, Z.; Chen, C.; Yang, D.; Zhou, K.; Wang, Y.; Jin, P.; Lin, J. Simulation for Multiwavelength Large-Aperture All-Silicon Metalenses in Long-Wave Infrared. *Nanotechnology* **2022**, *33*, 225203. [CrossRef]
7. Li, J.; Wang, Y.; Liu, S.; Xu, T.; Wei, K.; Zhang, Y.; Cui, H. Largest Aperture Metalens of High Numerical Aperture and Polarization Independence for Long-Wavelength Infrared Imaging. *Opt. Express* **2022**, *30*, 28882. [CrossRef]
8. Sun, S.; He, Q.; Xiao, S.; Xu, Q.; Li, X.; Zhou, L. Gradient-Index Meta-Surfaces as a Bridge Linking Propagating Waves and Surface Waves. *Nat. Mater.* **2012**, *11*, 426–431. [CrossRef] [PubMed]
9. Yu, N.; Genevet, P.; Kats, M.A.; Aieta, F.; Tetienne, J.-P.; Capasso, F.; Gaburro, Z. Light Propagation with Phase Discontinuities: Generalized Laws of Reflection and Refraction. *Science* **2011**, *334*, 333–337. [CrossRef] [PubMed]
10. Yin, Y.; Jiang, Q.; Wang, H.; Liu, J.; Xie, Y.; Wang, Q.; Wang, Y.; Huang, L. Multi-Dimensional Multiplexed Metasurface Holography by Inverse Design. *Adv. Mater.* **2024**, *36*, 2312303. [CrossRef] [PubMed]
11. He, H.; Peng, M.; Cao, G.; Li, Y.; Liu, H.; Yang, H. Higher-Order Poincaré Sphere Multiplexed Metasurface Holography for Optical Information Encryption. *Opt. Laser Technol.* **2025**, *180*, 111555. [CrossRef]
12. Zheng, G.; Mühlenbernd, H.; Kenney, M.; Li, G.; Zentgraf, T.; Zhang, S. Metasurface Holograms Reaching 80% Efficiency. *Nat. Nanotechnol.* **2015**, *10*, 308–312. [CrossRef]
13. Tang, S.; Li, X.; Pan, W.; Zhou, J.; Jiang, T.; Ding, F. High-Efficiency Broadband Vortex Beam Generator Based on Transmissive Metasurface. *Opt. Express* **2019**, *27*, 4281. [CrossRef]
14. Chen, D.; Yang, J.; He, X.; Yu, Y.; Zhang, Z.; Chen, H.; Zhang, Z.; Tan, Z.; Luo, H. Tunable Polarization-Preserving Vortex Beam Generator Based on Diagonal Cross-Shaped Graphene Structures at Terahertz Frequency. *Adv. Opt. Mater.* **2023**, *11*, 2300182. [CrossRef]
15. Tang, P.; Si, L.; Dong, L.; Wu, G.; Ma, T.; Bao, X.; Sun, H. Tunable Broadband Terahertz Graphene Metasurface for Complex-Amplitude Vortex Beam Generator and Hologram. *Opt. Laser Technol.* **2024**, *175*, 110874. [CrossRef]
16. Zhang, S.; Wen, F.; Zhai, M.; Li, Z.; Ye, H.; Zhang, H.; Gu, Y.; Lei, Y.; Wang, W.; Zhang, Y.; et al. Terahertz Dynamic Multiband Perfect Absorber with a Digital Coding Graphene-Diamond Metasurface. *Phys. Rev. Appl.* **2024**, *22*, 024004. [CrossRef]
17. Akselrod, G.M.; Huang, J.; Hoang, T.B.; Bowen, P.T.; Su, L.; Smith, D.R.; Mikkelsen, M.H. Large-Area Metasurface Perfect Absorbers from Visible to Near-Infrared. *Adv. Mater.* **2015**, *27*, 8028–8034. [CrossRef]
18. Yao, Y.; Shankar, R.; Kats, M.A.; Song, Y.; Kong, J.; Loncar, M.; Capasso, F. Electrically Tunable Metasurface Perfect Absorbers for Ultrathin Mid-Infrared Optical Modulators. *Nano Lett.* **2014**, *14*, 6526–6532. [CrossRef]
19. Fan, Z.-B.; Cheng, Y.-F.; Chen, Z.-M.; Liu, X.; Lu, W.-L.; Li, S.-H.; Jiang, S.-J.; Qin, Z.; Dong, J.-W. Integral Imaging Near-Eye 3D Display Using a Nanoimprint Metalens Array. *eLight* **2024**, *4*, 3. [CrossRef]
20. Cheng, W.; Wang, Y.; Zhang, Y.; Chen, H.; Lu, Z.; Zhao, F.; Wang, Y.; Wu, J.; Yang, J. Broadband Achromatic Imaging of a Metalens with Optoelectronic Computing Fusion. *Nano Lett.* **2024**, *24*, 254–260. [CrossRef] [PubMed]
21. Yao, J.; Lin, R.; Chen, M.K.; Tsai, D.P. Integrated-Resonant Metadevices: A Review. *Adv. Photonics* **2023**, *5*, 024001. [CrossRef]
22. Avayu, O.; Almeida, E.; Prior, Y.; Ellenbogen, T. Composite Functional Metasurfaces for Multispectral Achromatic Optics. *Nat. Commun.* **2017**, *8*, 14992. [CrossRef] [PubMed]

23. Aieta, F.; Kats, M.A.; Genevet, P.; Capasso, F. Multiwavelength Achromatic Metasurfaces by Dispersive Phase Compensation. *Science* **2015**, *347*, 1342–1345. [CrossRef] [PubMed]
24. Khorasaninejad, M.; Shi, Z.; Zhu, A.Y.; Chen, W.T.; Sanjeev, V.; Zaidi, A.; Capasso, F. Achromatic Metalens over 60 Nm Bandwidth in the Visible and Metalens with Reverse Chromatic Dispersion. *Nano Lett.* **2017**, *17*, 1819–1824. [CrossRef]
25. Arbabi, E.; Arbabi, A.; Kamali, S.M.; Horie, Y.; Faraon, A. Controlling the Sign of Chromatic Dispersion in Diffractive Optics with Dielectric Metasurfaces. *Optica* **2017**, *4*, 625. [CrossRef]
26. Chen, W.T.; Zhu, A.Y.; Sanjeev, V.; Khorasaninejad, M.; Shi, Z.; Lee, E.; Capasso, F. A Broadband Achromatic Metalens for Focusing and Imaging in the Visible. *Nat. Nanotechnol.* **2018**, *13*, 220–226. [CrossRef]
27. Wang, F.; Zhao, S.; Wen, Y.; Sun, J.; Zhou, J. High Efficiency Visible Achromatic Metalens Design via Deep Learning. *Adv. Opt. Mater.* **2023**, *11*, 2300394. [CrossRef]
28. Hou, L.; Zhou, H.; Zhang, D.; Lu, G.; Zhang, D.; Liu, T.; Xiao, S.; Yu, T. High-Efficiency Broadband Achromatic Metalens in the Visible. *Appl. Phys. Lett.* **2025**, *126*, 101704. [CrossRef]
29. Wang, Y.; Chen, Q.; Yang, W.; Ji, Z.; Jin, L.; Ma, X.; Song, Q.; Boltasseva, A.; Han, J.; Shalaev, V.M.; et al. High-Efficiency Broadband Achromatic Metalens for near-IR Biological Imaging Window. *Nat. Commun.* **2021**, *12*, 5560. [CrossRef]
30. Balli, F.; Sultan, M.; Lami, S.K.; Hastings, J.T. A Hybrid Achromatic Metalens. *Nat. Commun.* **2020**, *11*, 3892. [CrossRef] [PubMed]
31. Ou, K.; Yu, F.; Li, G.; Wang, W.; Chen, J.; Miroshnichenko, A.E.; Huang, L.; Li, T.; Li, Z.; Chen, X.; et al. Broadband Achromatic Metalens in Mid-Wavelength Infrared. *Laser Photonics Rev.* **2021**, *15*, 2100020. [CrossRef]
32. Zhou, H.; Chen, L.; Shen, F.; Guo, K.; Guo, Z. Broadband Achromatic Metalens in the Midinfrared Range. *Phys. Rev. Appl.* **2019**, *11*, 024066. [CrossRef]
33. Hou, M.; Chen, Y.; Li, J.; Yi, F. Single 5-Centimeter-Aperture Metalens Enabled Intelligent Lightweight Mid-Infrared Thermographic Camera. *Sci. Adv.* **2024**, *10*, eado4847. [CrossRef]
34. Lin, H.-I.; Geldmeier, J.; Baleine, E.; Yang, F.; An, S.; Pan, Y.; Rivero-Baleine, C.; Gu, T.; Hu, J. Wide-Field-of-View, Large-Area Long-Wave Infrared Silicon Metalenses. *ACS Photonics* **2024**, *11*, 1943–1949. [CrossRef]
35. Song, N.; Xu, N.; Shan, D.; Zhao, Y.; Gao, J.; Tang, Y.; Sun, Q.; Chen, X.; Wang, Y.; Feng, X. Broadband Achromatic Metasurfaces for Longwave Infrared Applications. *Nanomaterials* **2021**, *11*, 2760. [CrossRef]
36. Shi, X.; Meng, D.; Qin, Z.; He, Q.; Sun, S.; Zhou, L.; Smith, D.R.; Liu, Q.H.; Bourouina, T.; Liang, Z. All-Dielectric Orthogonal Doublet Cylindrical Metalens in Long-Wave Infrared Regions. *Opt. Express* **2021**, *29*, 3524. [CrossRef] [PubMed]
37. Sha, C.; Xiong, W.; Zhang, B.; Ding, J. Broadband Achromatic Mid-Infrared Metalens with Polarization-Insensitivity. *AIP Adv.* **2022**, *12*, 025123. [CrossRef]
38. Shang, H.; Zhang, M.; Sun, D.; Liu, Y.-G.; Wang, Z.; Liu, D.; Zeng, S. Optical Investigation of Chalcogenide Glass for On-Chip Integrated Devices. *Results Phys.* **2021**, *28*, 104552. [CrossRef]
39. Shang, H.; Sun, D.; Zhang, M.; Song, J.; Yang, Z.; Liu, D.; Zeng, S.; Wan, L.; Zhang, B.; Wang, Z.; et al. On-Chip Detector Based on Supercontinuum Generation in Chalcogenide Waveguide. *J. Light. Technol.* **2021**, *39*, 3890–3895. [CrossRef]
40. Song, J.; Pan, J.; Wan, L.; Chen, Z.; Zhu, Y.; Yang, Z.; Chen, Y.; Zhang, M.; Yi, X.; Li, Z. Ultrasound Measurement Using On-Chip Optical Micro-Resonators and Digital Optical Frequency Comb. *J. Light. Technol.* **2020**, *38*, 5293–5301. [CrossRef]
41. Zhu, Y.; Wan, L.; Chen, Z.S.; Yang, Z.; Xia, D.; Zeng, P.; Song, J.; Pan, J.; Feng, Y.; Zhang, M.; et al. Effects of Shallow Suspension in Low-Loss Waveguide-Integrated Chalcogenide Microdisk Resonators. *J. Light. Technol.* **2020**, *38*, 4817–4823. [CrossRef]
42. Hadibrata, W.; Wei, H.; Krishnaswamy, S.; Aydin, K. Inverse Design and 3D Printing of a Metalens on an Optical Fiber Tip for Direct Laser Lithography. *Nano Lett.* **2021**, *21*, 2422–2428. [CrossRef]
43. Lio, G.E.; Ferraro, A.; Ritacco, T.; Aceti, D.M.; De Luca, A.; Giocondo, M.; Caputo, R. Leveraging on ENZ Metamaterials to Achieve 2D and 3D Hyper-Resolution in Two-Photon Direct Laser Writing. *Adv. Mater.* **2021**, *33*, 2008644. [CrossRef]
44. Hu, Y.; Li, L.; Wang, R.; Song, J.; Wang, H.; Duan, H.; Ji, J.; Meng, Y. High-Speed Parallel Plasmonic Direct-Writing Nanolithography Using Metasurface-Based Plasmonic Lens. *Engineering* **2021**, *7*, 1623–1630. [CrossRef]
45. Fan, Z.-B.; Qiu, H.-Y.; Zhang, H.-L.; Pang, X.-N.; Zhou, L.-D.; Liu, L.; Ren, H.; Wang, Q.-H.; Dong, J.-W. A Broadband Achromatic Metalens Array for Integral Imaging in the Visible. *Light Sci. Appl.* **2019**, *8*, 67. [CrossRef]
46. Fan, Q.; Liu, M.; Yang, C.; Yu, L.; Yan, F.; Xu, T. A High Numerical Aperture, Polarization-Insensitive Metalens for Long-Wavelength Infrared Imaging. *Appl. Phys. Lett.* **2018**, *113*, 201104. [CrossRef]
47. Li, Q.; Ledoux-Rak, I.; Lai, N.D. Influence of Incident Beam Polarization on Intensity and Polarization Distributions of Tight Focusing Spot. *Adv. Device Mater.* **2015**, *1*, 4–10. [CrossRef]
48. Kennedy, J.; Eberhart, R. Particle Swarm Optimization. In *Proceedings of the ICNN'95—International Conference on Neural Networks, Perth, Australia, 27 November–1 December 1995*; IEEE: Piscataway, NJ, USA, 1995; Volume 4, pp. 1942–1948.
49. Clerc, M.; Kennedy, J. The Particle Swarm—Explosion, Stability, and Convergence in a Multidimensional Complex Space. *IEEE Trans. Evol. Comput.* **2002**, *6*, 58–73. [CrossRef]
50. Xia, C.; Liu, M.; Wang, J.; Wang, Y.; Zhang, S.; Lin, P.; Xu, T. A Polarization-Insensitive Infrared Broadband Achromatic Metalens Consisting of All-Silicon Anisotropic Microstructures. *Appl. Phys. Lett.* **2022**, *121*, 161701. [CrossRef]

51. Wu, H.; Yi, Y.; Zhang, N.; Zhang, Y.; Wu, H.; Yi, Z.; Liu, S.; Yi, Y.; Tang, B.; Sun, T. Inverse Design Broadband Achromatic Metasurfaces for Longwave Infrared. *Opt. Mater.* **2024**, *148*, 114923. [CrossRef]
52. Shan, D.; Xu, N.; Gao, J.; Song, N.; Liu, H.; Tang, Y.; Feng, X.; Wang, Y.; Zhao, Y.; Chen, X.; et al. Design of the All-Silicon Long-Wavelength Infrared Achromatic Metalens Based on Deep Silicon Etching. *Opt. Express* **2022**, *30*, 13616. [CrossRef] [PubMed]

**Disclaimer/Publisher's Note:** The statements, opinions and data contained in all publications are solely those of the individual author(s) and contributor(s) and not of MDPI and/or the editor(s). MDPI and/or the editor(s) disclaim responsibility for any injury to people or property resulting from any ideas, methods, instructions or products referred to in the content.